

Spatially resolved spectroscopy across stellar surfaces. V.

Observational prospects: Toward Earth-like exoplanet detection

Dainis Dravins¹, Hans-Günter Ludwig², and Bernd Freytag³

¹ Lund Observatory, Department of Astronomy and Theoretical Physics, Lund University, Box 43, SE-22100 Lund, Sweden
e-mail: dainis@astro.lu.se

² Zentrum für Astronomie der Universität Heidelberg, Landessternwarte, Königstuhl, DE-69117 Heidelberg, Germany
e-mail: hludwig@lsw.uni-heidelberg.de

³ Theoretical Astrophysics, Department of Physics and Astronomy, Uppsala University, Box 516, SE-75120 Uppsala, Sweden
e-mail: bernd.freytag@physics.uu.se

Received 26 November, 2020; accepted 1 February, 2021

ABSTRACT

Context. High-precision stellar analyses require hydrodynamic 3D modeling. Testing such models is feasible by retrieving spectral line shapes across stellar disks, using differential spectroscopy during exoplanet transits. Observations were presented in Papers I, II, and III, while Paper IV explored synthetic data at hyper-high spectral resolution for different classes of stars, identifying characteristic patterns for Fe I and Fe II lines.

Aims. Anticipating future observations, the observability of patterns among photospheric lines of different strength, excitation potential and ionization level are examined from synthetic spectra, as observed at ordinary spectral resolutions and at different levels of noise. Time variability in 3D atmospheres induces changes in spectral-line parameters, some of which are correlated. An adequate calibration could identify proxies for the jitter in apparent radial velocity to enable adjustments to actual stellar radial motion.

Methods. We used spectral-line patterns identified in synthetic spectra at hyper-high resolution in Paper IV from 3D models spanning $T_{\text{eff}} = 3964\text{--}6726\text{ K}$ (spectral types $\sim\text{K8 V}\text{--}\text{F3 V}$) to simulate practically observable signals at different stellar disk positions at various lower spectral resolutions, down to $\lambda/\Delta\lambda = 75,000$. We also examined the center-to-limb temporal variability.

Results. Recovery of spatially resolved line profiles with fitted widths and depths is shown for various noise levels, with gradual degradation at successively lower spectral resolutions. Signals during exoplanet transit are simulated. In addition to Rossiter-McLaughlin type signatures in apparent radial velocity, analogous effects are shown for line depths and widths. In a solar model, temporal variability in line profiles and apparent radial velocity shows correlations between jittering in apparent radial velocity and fluctuations in line depth.

Conclusions. Spatially resolved spectroscopy using exoplanet transits is feasible for main-sequence stars. Overall line parameters of width, depth and wavelength position can be retrieved already with moderate efforts, but a very good signal-to-noise ratio is required to reveal the more subtle signatures between subgroups of spectral lines, where finer details of atmospheric structure are encoded. Fluctuations in line depth correlate with those in wavelength, and because both can be measured from the ground, searches for low-mass exoplanets should explore these to adjust apparent radial velocities to actual stellar motion.

Key words. stars: atmospheres – stars: solar-type – techniques: spectroscopic – stars: line profiles – exoplanets: radial velocity – exoplanets: transits

1. Introduction

This project concerns the atmospheric structure and detailed spectra of solar-type stars, and detection schemes in searches for Earth-like exoplanets in orbits around them. It aims at recording high-resolution spectra across spatially highly resolved stellar surfaces and to identify signatures from surface features such as granulation or magnetically active regions. In Papers I, II, and III of this series (Dravins et al. 2017a,b, 2018), a method for such spatially resolved spectroscopy was elaborated and applied to observations of the G0 V star HD 209458, and the K1 V star HD 189733A (“Aloex”). Differential spectroscopy during exoplanet transits retrieves spectra from the stellar surface portions that temporarily become hidden during successive transit epochs. Tests of 3D hydrodynamic models of photospheric convection become possible through comparisons to synthetic spectral-line profiles at various center-to-limb positions, computed as temporal and spatial averages over their simula-

tion sequences. In Paper IV (Dravins et al. 2021), photospheric spectral-line shapes and shifts were examined in the 400–700 nm region from complete stellar spectra synthesized at hyper-high spectral resolution ($\lambda/\Delta\lambda > 1,000,000$), obtained from 3D hydrodynamic CO⁵BOLD simulations (Freytag et al. 2012; Ludwig et al. 2021). These spectral signatures encode the detailed properties of the dynamic stellar photosphere, and can serve as a diagnostic tool for testing and verifying hydrodynamic simulations for various classes of stars. Sufficiently developed models should be able to predict stellar microvariability in radial-velocity jittering and to identify possible proxies, such as could be measured in parallel in order to segregate stellar surface variations from its center-of-mass wobble induced by small orbiting exoplanets.

This Paper V examines the practical observability of specific spectral features (and their variability in time) when observed with realistic instrumentation. It is organized as follows: After the first introductory parts, Sect. 3 illustrates how suc-

sively lower spectral resolutions affect the observable spectral line shapes and shifts, Sect. 4 simulates the retrieval of spatially resolved spectra from exoplanet transit sequences at various noise levels, Sect. 5 shows the signatures of the Rossiter-McLaughlin type that exist in the remnant stellar light during an exoplanet transit, Sect. 6 examines the short-term temporal variability to identify spectral-line parameters that correlate with jittering in apparent radial velocity, and Sect. 7 outlines challenges and problems that have not yet been treated.

2. Spectral lines from realistic 3D models

While the overall feasibility of spatially resolved spectroscopy and the detection of specific 3D signatures was demonstrated in Papers I, II, and III, the finer details of hydrodynamic atmospheric structure are encoded in the different responses in various types of lines, where the practical observability is less obvious. Paper IV exploited noise-free synthetic spectra at hyper-high resolution to understand how many of these characteristic patterns in Fe I and Fe II lines remain detectable in also realistically complex stellar spectra, where practically all blending and other lines are included. Line profiles and bisector shifts between stronger and weaker lines reflect properties at different atmospheric heights and change between stars with different gradients in their line-forming volumes. Higher-excitation lines may preferentially form in hotter regions than low-excitation lines although components of neutral atomic species from the hottest locations may be weakened due to deviations from local thermodynamic equilibrium (NLTE effects). There, increased ultraviolet flux can ionize the line-forming layers above; in some cases, there are prospects for studying these effects separately for the hotter granules and the intergranular lanes. Time variability from 3D atmospheres implies correlations between various spectral-line measures, suggesting further detailed tests of 3D models.

2.1. The quest for Earth-like exoplanets

An outstanding challenge is to find closely Earth-like exoplanets, whose sizes, masses, and orbits are comparable to the terrestrial values. One plausible path toward their detection is to identify the wobble in radial velocity caused by the stellar motion around the system barycenter, induced by the orbital motion of the planet(s). Although the tiny amplitude induced by the Earth on the Sun amounts at most to only 0.1 m s^{-1} (e.g., Hall et al. 2018), instrument precisions are now beginning to reach these levels (Blackman et al. 2020; Brewer et al. 2020; Cale et al. 2019; Gilbert et al. 2018; Langellier et al. 2020; Lo Curto et al. 2012; Metcalf et al. 2019; Pepe et al. 2014; Petersburg et al. 2020; Probst et al. 2020; Robertson et al. 2019; Roy et al. 2016; Strassmeier et al. 2018a; Suárez Mascareño et al. 2020; Wilken et al. 2012; Zhao et al. 2021) and they are design criteria for future instruments (Halverson et al. 2016; Pasquini et al. 2010; Plavchan et al. 2019; Zerbi et al. 2014). The main limitations are no longer technical but lie in understanding the complexities of atmospheric dynamics and spectral line formation, manifest both as a jitter of the apparent radial velocity and as a flicker in photometric brightness (Cegla 2019; Fischer et al. 2016).

In the Sun and solar-type stars, with maybe a million granules covering their disks, wavelength positions of photospheric absorption lines jitter on a level of perhaps $\sim 2 \text{ m s}^{-1}$ (Collier Cameron et al. 2019; Dumusque et al. 2015, 2020), an order of magnitude that is consistent with the averaged random variability of a million granules, each with an amplitude of \sim

km s^{-1} . Photometric flickering in irradiance is analogous: A typical brightness contrast of $\sim 20\%$ in each granule reduces to $\sim 2 \cdot 10^{-4}$ after averaging over a million random locations (e.g. Némec et al. 2020). The amplitude diminishes with increased averaging times (Bastien et al. 2016; Cranmer et al. 2014). Further phenomena such as starspots or faculae are adding to the confusion (İşik et al. 2020; Korhonen et al. 2015; Lagrange et al. 2010; Lisogorskyi et al. 2020; Meunier et al. 2010; Milbourne et al. 2019; Norris et al. 2017).

The radial-velocity wobble induced by a small exoplanet is much smaller than stellar microvariability, therefore effects of the latter must somehow be calibrated and corrected for. Numerous authors have studied empirical correlations between various stellar activity indices and corresponding excursions in apparent radial velocity (e.g., Cegla et al. 2014, 2019; Collier Cameron et al. 2020; de Beurs et al. 2020; Dumusque 2016; Feng et al. 2016; Haywood et al. 2016; Hojjatpanah et al. 2020; Kosiarek & Crossfield 2020; Lanza et al. 2019; Luhn et al. 2020a; Marchwinski et al. 2015; Meunier et al. 2010, 2015, 2017b; Miklos et al. 2020; Oshagh et al. 2017; Sulis et al. 2020a; Tayar et al. 2019; Thompson et al. 2020).

Most studies have considered the Sun seen as a star, where activity patterns on the visible disk are known from observations from the ground (e.g., sunspots, magnetic fields, and chromospheric Ca II H & K emission) or from space (photometric irradiance and ultraviolet flux). Numerous techniques have been applied, analyzing mathematical correlations between various quantities or applying neural networks. Temporal filtering can distinguish between evolutionary and recurrence timescales, for instance, active-region growth times versus stellar rotation periods. However, even if solar variations can thus be traced and a mitigation of radial-velocity signals is reached, the same means are not available for other stars. Relations between stellar photometric flicker and wavelength jitter confirm the impact of magnetic activity on apparent radial velocities but the relations vary among different stellar types and depend on metallicity (Tayar et al. 2019).

Although various solar-calibrated relations may be applied to also other stars, these correlations do not yet reach sufficient predictability to permit the identification of low-mass exoplanets in Earth-like orbits. We suspect that such types of empirical correlations may not be able to approach the required precisions, and a different approach would therefore be needed.

This could be based upon a detailed physical modeling of temporal variability in stellar atmospheres, precisely predicting how various types of thermal and magnetic variability are manifest in the details of the emergent and observable spectrum. It is enabled by the recent feasibility to simulate entire and complete time-variable stellar spectra including practically all spectral lines, and possible for different classes of stars.

If these processes can be adequately understood from more basic principles, it should become possible to identify which spectral parameters in what spectral lines should best be observed in different stars, and what observational precision will be required to identify small exoplanets as well. Recent efforts in this direction for the Sun seen as a star include the extraction of radial-velocity data from separate sublists of lines with different depths (Miklos et al. 2020) and the study of how extended spectral portions differ at epochs of magnetically more or less active periods (Thompson et al. 2020).

Fluctuations in hydrodynamic atmospheres affect many spectral-line parameters in concert. Line components originating from hotter granules in their normally rising motion become locally blueshifted and carry higher photon fluxes due to brighter

continuum intensities. Steeper gradients in density and temperature above granules tend to cause increased strengths of absorption lines. Lower opacity in cooler intergranular lanes may enable lines to form over greater depths, and to experience vertical velocity gradients, which leads to more pronounced line asymmetries. All these dependences may further vary among lines with different temperature sensitivities, for example, high-excitation lines from ionized species versus lines from easily dissociated molecules (e.g., Allende Prieto et al. 2002; Chiavassa et al. 2018; Dravins & Nordlund 1990; Nordlund et al. 2009; Trampedach et al. 2013).

If it can be adequately understood which parameters can serve as proxies for jittering in radial velocity (and especially if these quantities can be measured from the ground), it should enable the push toward sub- m s^{-1} precisions, as required for exoEarth detections. It is clear that there is additional information content in individual spectral lines, as compared to statistically averaged correlation functions and such (Dumusque 2018; Cretignier et al. 2020), but how much that can be retrieved must depend on how precisely each particular spectral line or line group can be measured. Various correlations among parameters may be searched from extended 3D simulations and could be verified in low-noise observations of bright stars. When these correlations are understood, they might be used in radial-velocity searches for low-mass exoplanets to adjust measured radial-velocity values to true stellar radial motion, at least for the displacements caused by thermally driven granulation. Additional complexities are to be considered separately, in spatially resolved spectroscopy of magnetically active regions and of starspots.

2.2. Transit light source effects

A further motivation for studying spatially resolved stellar spectra is that atmospheric properties of any transiting exoplanet must be deduced as subtle differences against the background stellar spectrum, which thus must be precisely known. This requires a knowledge of the varying stellar line profiles at the positions along the transit path of the planet (Apai et al. 2018; Rackham et al. 2018, 2019; Yan et al. 2017); these are the features that are filtered through the exoplanetary atmosphere, not the spectrum of the flux from the full stellar disk. Additionally, the spectrum of the stellar flux that remains during exoplanetary transit (then displaying the Rossiter-McLaughlin effect) depends not only on stellar rotation but is also modified by the change in line profiles across the stellar disk.

3. Finite spectral resolution

All data in Paper IV were at the original hyper-high spectral resolutions $\lambda/\Delta\lambda > 1,000,000$. Although these levels are required to (almost) fully resolve line asymmetries and shifts, this will likely not be available for stellar observations in the near future. In this section we examine the spectral-line signatures that are preserved at the lower spectral resolutions that are commonly achievable.

Spectra at an order of magnitude lower resolution of $\lambda/\Delta\lambda \sim 100,000$ may be adequate to identify the existence of almost all spectral lines but not to reveal their precise line shapes. The effects of finite resolution can be appreciated by noting that because the relevant width of a typical photospheric line may be about 12 km s^{-1} , a resolution of $100,000$ (3 km s^{-1}) provides four resolution points across that line profile, while a resolution of $300,000$ (1 km s^{-1}) gives 12 points. A bisector is obtained by

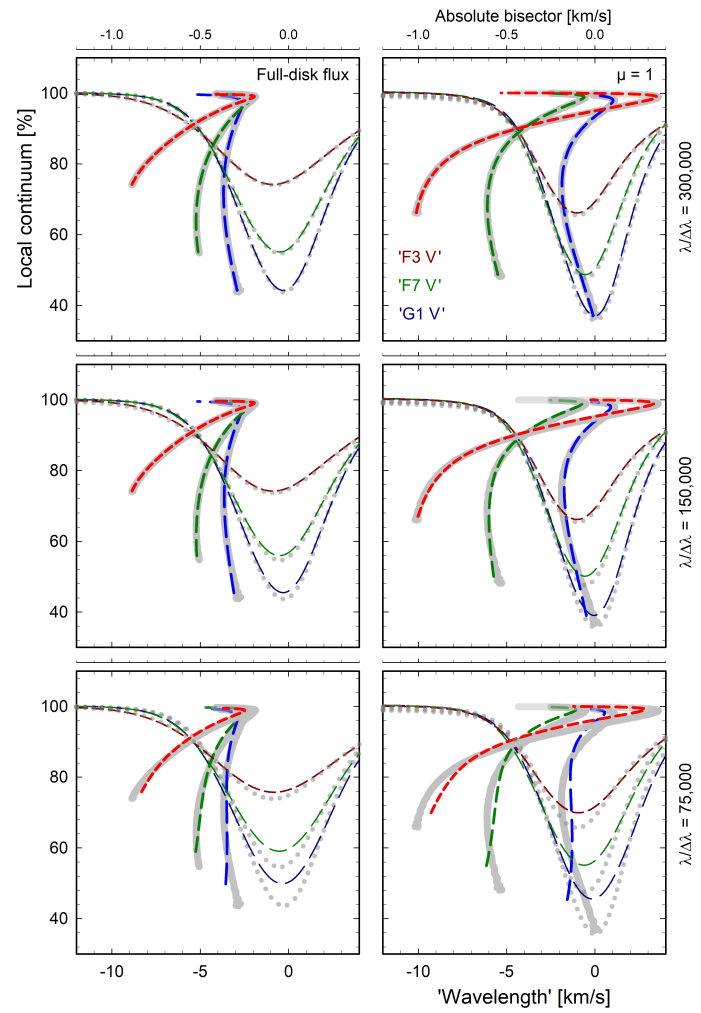


Fig. 1. Effects of decreasing spectral resolution on line profiles (axes at the bottom) and their bisectors (tenfold expanded axes at the top) for a representative spectral line. From the top down, three rows show the Fe I $\lambda 539.8286 \text{ nm}$ line for $\lambda/\Delta\lambda = 300,000$, 150,000, and 75,000. The left column shows data for integrated full-disk flux, and the right column that for stellar disk center ($\mu = 1$). The same Fe I line is shown in models for 'F3 V', 'F7 V', and 'G1 V' as short-, medium-, and long-dashed lines (red, green, and blue). Each frame also shows profiles and bisectors at the original hyper-high spectral resolution, marked as dotted gray and solid gray curves.

averaging pairs of resolution points in the shortward and longward flanks of the line. The number of data points on the bisector is thus half of these numbers, in these examples 2 and 6, respectively. With very few independent points, we cannot define much more than a straight line, indicating the bisector wavelength position and its slope (i.e., the sense of line asymmetry). To detect any curvature on a bisector requires several photometric measurements across the relevant portions of a line. The exact requirements depend on the intrinsic width of the lines, and are less stringent for broader lines (such as the line in Fig. 1). The degradation of bisector shapes with dropping resolving power is well illustrated for observed solar lines when the resolution is gradually decreased from 700,000 to 100,000 (Löhner-Böttcher et al. 2018, 2019).

Any spectral synthesis is limited not only by computational sophistication but also by the (non-)availability of precise laboratory data for spectral lines from all species, including components from different isotopes or hyperfine structure patterns.

A circumvention of these problems in comparing modeling with observations suggests preferentially studying atomic species that are dominated by one isotope that is even-even in its proton-neutron numbers, so that its nuclear spin and thus hyperfine splitting is zero. In addition, this species should be of high mass, minimizing the thermal broadening of the lines, to better segregate effects of photospheric gas flows. Similar to other studies, the preferred atomic species is iron. Its dominant isotope, $^{26}\text{Fe}^{56}$ has a (terrestrial) abundance of 91.7% while a few isotopes with lighter and heavier mass exist: $^{26}\text{Fe}^{54}$ has 5.8%, $^{26}\text{Fe}^{57}$ has 2.1%, and $^{26}\text{Fe}^{58}$ has 0.3% (de Laeter et al. 2003). The nuclear spin I and hyperfine splitting are zero for $^{26}\text{Fe}^{54}$, $^{26}\text{Fe}^{56}$, and $^{26}\text{Fe}^{58}$ and small for $^{26}\text{Fe}^{57}$ ($I = \frac{1}{2}$). Thus, asymmetries induced by isotope shifts and hyperfine structure should be negligible. When adequate laboratory data and ensuing modeling become available, it should be possible to extract additional information from the detailed behavior of lines from species whose hyperfine splitting spans ranges corresponding to photospheric velocity amplitudes; for instance, patterns for $^{25}\text{Mn}^{55}$ of 100% abundance and $I = \frac{5}{2}$, extend over ~ 10 pm (~ 5 km s $^{-1}$). In the following, however, we limit the discussion to the Fe I and Fe II line selections described in Paper IV.

3.1. Observational possibilities

Anticipating future observations, we now examine the signatures in spectral lines that might realistically be observed at resolutions corresponding to those of actual stellar spectrometers at major telescopes. Several precision instruments realize $\lambda/\Delta\lambda \sim 100,000$; resolutions of about 200,000 are possible with ESPRESSO at the ESO VLT¹ (Pepe et al. 2014, 2021; González Hernández et al. 2018) but extended spectral ranges approaching $\lambda/\Delta\lambda \sim 300,000$ are currently only offered by PEPSI at the LBT² (Strassmeier et al. 2015, 2018b). Actual performance comparisons have been made by Adibekyan et al. (2020), Benatti (2018), and Crossfield (2014). Despite the ample photon fluxes in future extremely large telescopes, conventional spectrometer designs will likely not reach equally high values, constrained by the difficulty to match diffraction grating sizes to the large image scales. This holds for HIRES on the ELT³ (Marconi et al. 2016, 2021; Zerbi et al. 2014) or concepts such as CODEX⁴ (Pasquini et al. 2010). Spectrometers with adaptive optics fed by single-mode fibers might be able to circumvent this limitation (Bechter et al. 2018; Beckers et al. 2007; Crass et al. 2019; Jovanovic et al. 2019). A few other instruments have occasionally been used to record limited spectral segments at even higher resolutions, but they are not adapted to extended spectral regions. The resolution values typically refer to the instrumental profile full width at half maximum, which the detector normally samples with at least two detector pixels.

Our models have the temperatures $T_{\text{eff}} = 3964, 4982, 5700, 5865, 6233$, and 6726 K, and similar to Paper IV (its Table 1), these are referred to with their approximate corresponding spectral types as ‘K8 V’, ‘K2 V’, ‘G2 V’, ‘G1 V’, ‘F7 V’ and ‘F3 V’.

¹ ESPRESSO, the Echelle SPectrograph for Rocky Exoplanets and Stable Spectroscopic Observations, at VLT, the Very Large Telescope of ESO, the European Southern Observatory

² PEPSI, the Potsdam Echelle Polarimetric and Spectroscopic Instrument at LBT, the Large Binocular Telescope

³ HIRES, the High Resolution Spectrograph planned for ELT, the Extremely Large Telescope of ESO

⁴ CODEX, COsmic Dynamics and EXo-earth experiment, a spectrograph originally proposed for the then OWL, Overwhelmingly Large Telescope, project

Fig. 1 shows the successive degradation of one strong line (Fe I $\lambda 539.8286$ nm) when shifting from hyper-high resolution to the observationally more realistic values of 300,000, 150,000 and 75,000. Three stellar models are shown for integrated full-disk spectra and for the stellar disk center. Most of the line signatures are preserved at $\lambda/\Delta\lambda = 300,000$ but below $\sim 150,000$, line asymmetries become distorted (as expected).

Observed full-disk spectra will display additional broadening arising from (rigid or differential) stellar rotation and possible large-scale surface oscillations or flows. Spatially resolved spectra are free from these effects and will instead be shifted in wavelength by amounts corresponding to the components of stellar rotation along the line of sight at each particular position of the transiting planet (Papers II and III). We recall that the hydrodynamic simulations do not entail any fitting parameters. In particular, concepts such as turbulence do not enter – spectral line shapes result from their formation within the computed volumes of gas flows at different optical depths along the line of sight.

3.2. Fitting line parameters

In realistic observations, noise levels constrain the detailed analysis of line profiles and only some line-averaged measures might be obtained from some fitting, smoothing, or averaging. Fig. 2 shows how such fitted widths and shifts are altered, depending on the achieved spectral resolution. As an approximation, the profiles (in this section still assumed to be noise-free) at each spectral resolution were fit with five-parameter Gaussian-type functions of the type $y_0 + a \cdot \exp[-0.5 \cdot (|x - x_0|/W)^c]$, yielding W as a measure of the line width, and x_0 for the central wavelength. Although the profiles are not precisely Gaussian, these simple functions appear reasonable to use in fitting imperfect data. Different functions have previously been tested (Lorentzian, etc.), but it was found that plain Gaussian varieties gave robust estimates for the basic line parameters. A fitting like this is relevant in cases of noisy data when full line profiles cannot be retrieved, and then only simpler fitting functions are likely to be justified. The parameters of line-width measure and (average) wavelength position appear to be the most easily measurable quantities, also for the center-to-limb dependences in spatially resolved spectra. In particular, for many stars, the line widths are expected to increase toward the limb, providing a quantitative measure that the greater horizontal motion amplitudes contribute more Doppler broadening.

In Fig. 2 it is striking that much of the signatures also remains at lower spectral resolutions. When the value has reached $\lambda/\Delta\lambda \sim 150,000$, extending to even higher resolutions brings only very slight changes in parameters that are fit to the overall line profiles.

The data in Fig. 2 are for representative lines of different strength, which is the one factor (rather than excitation potential or wavelength region) that appears to be foremost in affecting the spectral parameters. Differently strong lines are prevalent in different parts of the spectrum: statistics of atomic energy levels dictate that most strong lines from neutral metals appear in the blue or violet parts, while weaker transitions are common in the red and infrared. In general, convective signatures can be expected to be weaker at longer wavelengths because any temperature difference between thermally radiating hot and cool elements causes a lower intensity contrast in the (infra)red, diminishing the statistical imbalance between blueshifted line components from hot granules and redshifted contributions from intergranular regions (e.g., Asplund et al. 2000). A caveat is that spe-

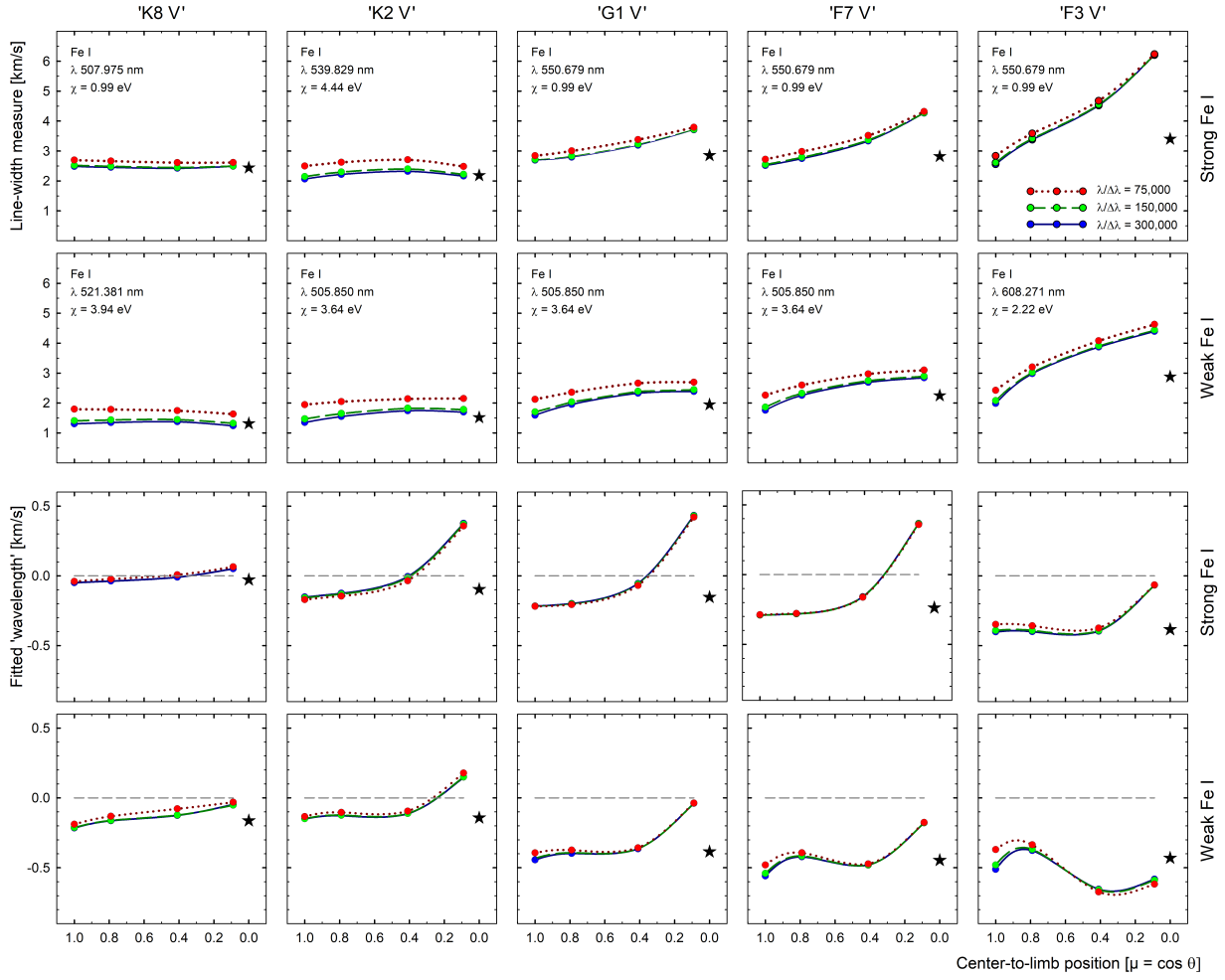


Fig. 2. Parameters obtained from fitting full line profiles at various spectral resolutions in different stars. Top rows: Fitted line widths for one weak and one strong line at different stellar disk positions. Bottom rows: Corresponding wavelength shifts. The values were obtained from fitting five-parameter Gaussian-type functions to the line profiles. Black stars denote values for integrated full-disk flux from 3D models at full hyper-high spectral resolution. Solid curves with blue symbols denote $\lambda/\Delta\lambda = 300,000$, dashed lines with green symbols show 150,000, and dotted curves with red symbols plot the lowest resolution of 75,000.

specific signatures might appear due to locally different atmospheric opacity in specific regions, however.

Single numbers for line width and wavelength are not uniquely defined measures, however, but depend on exactly how the fit is made, and with what type of weighting. For example, a wavelength measure may depend on whether the value is obtained from a fit to the central or more extended parts of the profile, or perhaps made with some correlation template that gives increased weight to steeper intensity gradients. For the more general question of quantifying spectral resolution in astronomical spectra, see Robertson (2013).

4. Reconstructed profiles from noisy observations

To reconstruct high-resolution spectra from behind the small areas covered by a transiting planet requires signal-to-noise ratios (S/N) much higher than commonly available in individual spectral exposures. As detailed in Papers I, II, and III, the requirements limit usable observations to spectra with the highest-fidelity from high-resolution spectrometers. For example, a S/N in the reconstructed spectrum of about 100, extracted from $\sim 1\%$ of the total stellar signal, requires an original S/N of about 10,000. The remedy applied in Papers II and III was to form averages over numerous lines of similar strength that form under

similar conditions in the stellar atmosphere, and are expected to display similar characteristics. These possibilities, however, may be limited to certain spectral regions or to cooler stars with particularly rich spectra.

To appreciate the levels of spectral quality that can be realized at different levels of observational noise, simulated observations were calculated at different spectral resolutions and for noise levels bracketing values that provide meaningful reconstructions. The area of a transiting planet, A , was assumed equal to 1.5% of the stellar disk for each stellar model, roughly corresponding to a Jupiter-size object. At each disk position, the temporarily hidden spectral signal S equals that from the full stellar disk (outside transit) minus that from the unobsured portions, its normalization in intensity set by A ; thus: $S_{\text{hidden}} = (S_{\text{outside-transit}} - S_{\text{in-transit}})/A$. Because the reconstructions involve dividing subtracted spectra by the low values of A , the noise is correspondingly enhanced. For a more detailed discussion of the steps in reconstructing spatially resolved profiles, see Paper II (e.g., its Fig. 9). Spectral reconstructions like this were here simulated from observations at spectral resolutions $\lambda/\Delta\lambda = 600,000$, 300,000, 150,000 and 75,000, sampled by spectrometers with two pixels per spectral resolution element. Random photometric noise was assumed with its standard deviation proportional to

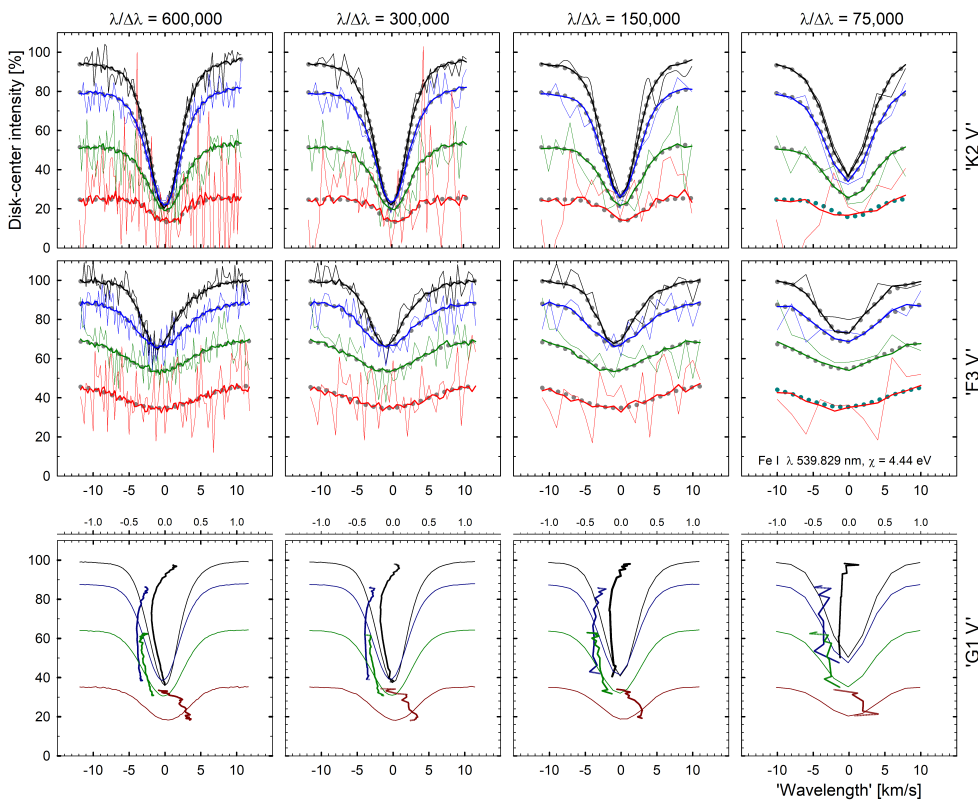


Fig. 3. Simulated noise in spatially resolved line profile reconstructions from observations during an exoplanet transit. Columns from left to right show reconstructions from resolutions $\lambda/\Delta\lambda = 600,000, 300,000, 150,000$ and $75,000$, sampled with two pixels per spectral resolution element. The two top rows show a cooler ‘K2 V’ and a hotter ‘F3 V’ star, differing in line strengths, widths, and limb darkening. Photometric noise levels during transit in the spectral continuum are: $\sigma = 0.01\%$ (thin line) and 0.001% (bold). Noise-free profiles at each resolution are plotted as gray dots. Inside each frame and top down, profiles are for disk center positions $\mu = 1, 0.79, 0.41$, and 0.09 . Bottom row: Reconstructed profiles at the extremely low noise level of $\sigma = 0.0001\%$, which is required to also recover well the bisectors (tenfold expanded scale at top).

the square root of the flux in each pixel, and for exposures during transit, set to $\sigma = 0.01\%$, 0.001% , and 0.0001% of the spectral continuum. Because the stellar reference spectrum from outside the transit can be much better determined than those from brief exposures during transit, its noise level was set a factor of ten lower. These simulated line-profile reconstructions are shown in Fig. 3

Although the same line, Fe I $\lambda 539.82860$ nm, was used for all three stellar models ‘K2 V’, ‘G1 V’, and ‘F3 V’, the greater limb darkening for lower stellar temperatures has a certain effect on the profile reconstructions away from disk center because the signal from a planet away from disk center is weaker. The noise levels of 0.01% and 0.001% , in the top rows of Fig. 3 illustrate the range within which meaningful reconstructions of line profiles can be performed. These are adequate to obtain line-integrated parameters such as widths, depths and wavelength shifts, even if line profile shapes were lost (cf. Fig. 2). The actual reconstructions in Papers II and III were made at roughly comparable (or slightly worse) noise levels. The more demanding recovery of detailed line profile shapes and their precise bisectors will require both a very high spectral resolution and an extremely low noise level, as illustrated in the bottom row for a continuum noise $\sigma = 0.0001\%$ ($S/N = 10^6$), which might be approachable after extensive stacking of lines and exposures using future instruments on extremely large telescopes.

The role of different planet sizes should be recognized. Realistic line-profile reconstructions demand transit observations of large planets, for instance, Jupiter-size, covering $\sim 1\%$ of the disk of solar-type stars. Not only is this to satisfy the spectrophotometric requirements but also to provide adequate averaging over stellar surface inhomogeneities because such a planet covers $\sim 10,000$ granules out of the total $\sim 10^6$ granules that are present on such stars. A smaller planet would give not only a weaker signal in its differential spectroscopy between transit epochs but

also generate more astrophysical noise because the averaging area across stellar surface structures is smaller.

We recall that a plausible method for finding small planets is to try to identify the radial-velocity wobble of the host star as it moves in a reflex motion with the planet orbiting their common barycenter. Regardless of instrumental precision, such radial-velocity data have to be corrected to segregate fluctuations arising in the stellar atmosphere from the smaller variations induced by a possible small planet. Spatially resolved spectra retrieved from transits of large planets can be used to verify and constrain 3D simulations and these models can then be used to predict and calibrate spectral signatures of the host star, such as its apparent radial-velocity variations. However, it is not realistic to observationally retrieve stellar atmospheric properties from transits of Earth-size planets, covering only $\sim 10^{-4}$ of the stellar disk. In the following sections, we consider various types of simulated observations during, and outside planetary transits.

5. Rossiter-McLaughlin-type signatures

During the transit of an exoplanet across a rotating star, it selectively hides different portions of the stellar surface, where the local rotational velocity vector is toward or away from the observer. Thus, part of the blue- or redshifted photons are removed from the integrated stellar flux, whose averaged wavelength then appears slightly red- or blueshifted. The effect has been measured for numerous exoplanets, where measurements of this Rossiter-McLaughlin effect enable determining the geometry of the projected path of the exoplanet (Albrecht 2012; Perryman 2018; Winn 2011).

However, in addition to the line displacements due to obscured line contributions shifted by stellar rotation, a contribution comes from the intrinsic center-to-limb changes of stellar wavelengths caused by convective shifts, as previously evaluated by Cegla et al. (2016), Reiners et al. (2016), Shporer & Brown

(2011) and Yan et al. (2015a,b, 2017). In Fig. 4 we show detailed calculations for one line (the same as in Fig. 1), for four different stellar models, not only for this usual wavelength displacement but also for the concurrent changes in line widths and depths. A Jupiter-class exoplanet, covering 1.5% of each stellar disk was assumed, and profiles of the Fe I λ 539.8286 nm were fit with five-parameter Gaussians as above, in the resulting spectrum of the full-disk flux minus what is obscured by the planet at each respective disk position. While this example is for a rather strong Fe I line at the full hyper-high spectral resolution, the patterns are quite similar at lower resolutions as well, and also for other lines of comparable strength. The wavelength shifts are absolute but gravitational redshifts are neglected. The qualitative behavior can be readily understood: Lines are narrowest and deepest at disk center and when the planet obscures this region, the line width of the remaining stellar flux becomes broader, and the line depth shallower. The run of wavelength shifts is more complex because line asymmetries and convective line shifts are not necessarily monotonic with limb distance (Fig. 2).

6. Temporal flickering and jittering

The signatures discussed so far have been temporal averages but further details about stellar surfaces are encoded in their temporal variability. Stellar surface dynamics cause flickering in irradiance and photometric colors, and jittering in spectral line wavelengths, widths, shapes and depths. Although light from full stellar disks forms as the mean over perhaps a million granules, averaging over random structures decreases the signal by only the square root of their number, a slowly changing function. Full-disk flickering in broadband light retains amplitudes that are measurable by precision photometry from space. In temporal power spectra, granulation is detected on characteristic timescales, different from those of oscillations or stellar rotation, for instance. Details depend on stellar spectral type, are possible to model, and inversely, can be used to infer stellar properties from the observed flickering (Bastien et al. 2016; Cranmer et al. 2014; Kallinger et al. 2014; Lundkvist et al. 2021; Pande et al. 2018; Samadi et al. 2013a,b). Understanding full-disk flickering is also essential to appreciate the noise floor for exoplanet transits in current and future space photometry missions (Morris et al. 2020a; Sarkar et al. 2018; Sulis et al. 2020b).

Sharper diagnostics for the finer details of stellar atmospheres exist in the temporal variability of spectral lines, especially versatile when simultaneous fluctuations can be monitored in different types of lines. Variability that does not require data from space but can be recorded with instrumentation from the ground is particularly relevant. During instances when there happen to be particularly many bright granules on the stellar disk, more contributions of blueshifted line components from rising gases in the bright granules are expected, causing an enhanced convective blueshift. At the same time, the augmented irradiance implies an increased temperature and a bluer photometric color. Locally augmented irradiance may imply locally strengthened atmospheric gradients with ensuing changes to spectral line strengths. In this situation, photometric brightness, color, or some spectral-line parameter might be used as a proxy for excursions in apparent radial velocity and then be applied in order to adjust it to the physical stellar motion. To observationally explore and confirm these correlated relations, very bright stars where low-noise spectra can be obtained, would need to be observed first before the relations would be applied to exoplanet hosts.

6.1. Line profile variability

We examined the short-term spectral-line variability as computed from the temporal evolution in the simulation volumes. Eventually, it should become possible to study the temporal wavering of complete stellar spectra and to identify which line selections, spectral filters, correlation functions or other measures could best extract specific information on processes in diverse atmospheric structures at different atmospheric heights.

The discussion in this section, however, is limited to properties of single and idealized spectral lines. Analogous to synthetic data presented in Papers I, II, and III, these are isolated Fe I lines at λ 630 nm, shown here for two different excitation potentials $\chi = 1$ and 5 eV, and for three different line strengths. These are the data entering Figs. 5, 6, and 7. Their parameters bracket those of typical lines in spectra of respective spectral types while not intended to model any specific real line. With a single isolated line, its temporal response can be separated in a cleaner manner, without possible contamination from other line-formation effects (such as changing strengths of weak blending lines). Of the wavering line properties, the jittering in radial velocity is the primary quantity that needs to be calibrated in the search for Earth-like exoplanets, and this is shown in particular for a solar model, for which observational tests should be possible using already existing observations (e.g., Dumusque et al. 2020).

The character of temporal variability is illustrated in Fig. 5. Each superposed line profile for each of some 20 instances in time is formed as the average over thousands of spatial points across the simulation area (Table A.1 in Paper IV). These instances were selected to be sufficiently separated in time to ensure largely uncorrelated flow patterns between successive samples. These spatially averaged profiles do not (by far!) reveal the full spectral variability across stellar surfaces. This full variability is substantial and spatially resolved profiles can be distorted into grossly asymmetric shapes and may occasionally even become double-bottomed when the trail of line formation has passed through differentially moving inhomogeneities (e.g., Asplund 2005; Asplund et al. 2000; Bergemann et al. 2019; Chiavassa & Brogi 2019; Dravins & Nordlund 1990). The categorization of these variegated features probably would be confusing, therefore we use sufficiently extended spatial averages, where the line profiles already start to closely resemble the final ones, and where ordinary fitting can be applied to obtain readily understandable quantities for line width, depth and wavelength shift.

Fig. 6 shows the jittering range of the wavelength shifts for differently strong lines in three models, at four different disk positions of $\mu = 1, 0.87, 0.59$, and 0.21 as a function of the instantaneous irradiance from the simulation volume (normalized to the time-averaged flux at each respective stellar disk center). For the solar model ('G2 V'), the fluctuation amplitudes tend to increase from disk center toward the limb, especially for the weak line, while in the hotter 'F3 V' star, no such tendency is seen. This is apparently connected with the transition from partially hidden granulation in the Sun to more naked granulation in F stars. The full amplitude of solar granulation is encountered only very deep in the photosphere (even slightly below the visible surface), which is barely reached by even very weak lines in the optical. With the convective patterns rapidly changing with height, lines formed under marginally different conditions may already show dissimilar signatures. For F-type stars, with the full granulation contrast in optical view, these differential effects are much weaker, even though the convection as such is more vig-

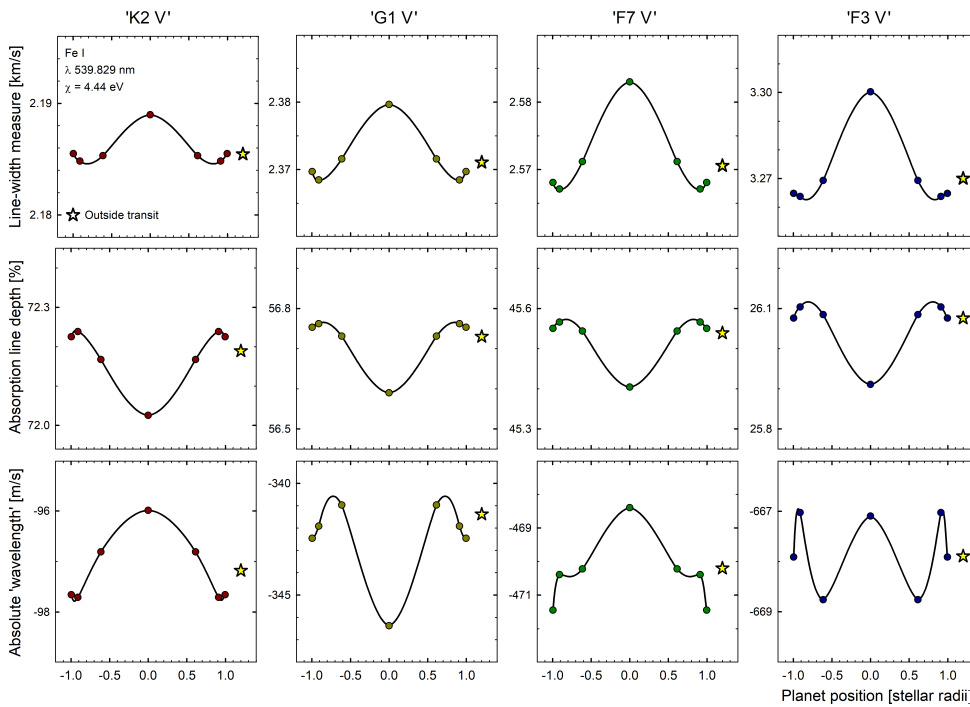


Fig. 4. Rossiter-McLaughlin-type signatures during the transit across a stellar diameter of an exoplanet covering 1.5% of the stellar disk, caused by center-to-limb changes in line profiles in the absence of stellar rotation. Columns left to right show the ‘K2 V’, ‘G1 V’, ‘F7 V’, and ‘F3 V’ models. Values for spectral-line widths, depths and wavelength shifts were obtained by fitting Fe I $\lambda 539.8286$ nm profiles with the planet at different disk positions. Line depths are in units of the local spectral continuum at each planetary transit position. Star symbols show full-disk values outside transit. Wavelength shift values are absolute but gravitational redshifts are neglected.

orous. In the cooler K-type stars, the full amplitude of granular convection largely remains hidden somewhat beneath the optically visible surface, and as a consequence, the convective wavelength shifts and their variations are much smaller. In order to show their minuscule jittering, the scale for the ‘K8 V’ star in Fig. 6 is expanded tenfold relative to that for the other stars.

6.2. Proxies for jitter in radial velocity

Searches for low-mass exoplanets would clearly benefit when some practically measurable quantities were identified that could be used to correct short-term excursions in apparent stellar radial velocity. A considerable effort has been made in studying the Sun as a star and in searching for statistical relations between various parameters of solar and stellar variability, including work by Cegla et al. (2019), Collier Cameron et al. (2019, 2020), de Beurs et al. (2020), Dumusque et al. (2015, 2020), Haywood et al. (2016), Lanza et al. (2016, 2019), Maldonado et al. (2019), Marchwinski et al. (2015) and Thompson et al. (2020), and references therein. These studies used various statistical approaches to search for possible correlations and empirical proxies for radial-velocity fluctuations. Considerations of other spectral types include Dumusque et al. (2011a) and Meunier et al. (2010, 2017a,b).

Precision photometry from space reveals the presence of granulation as flickering in brightness, with both observed and modeled connections between its temporal power spectra and stellar spectral type. In particular, flickering in brightness correlates with excursions in apparent radial velocity (Cegla et al. 2014; Hojjatpanah et al. 2020; Oshagh et al. 2017). However, securing space photometry simultaneously with spectroscopic radial-velocity surveys might be problematic although such photometry could select specific targets of particularly low flickering level, presumably with also low levels of radial-velocity jitter (Luhn et al. 2020a,b; Tayar et al. 2019).

In this project, however, we did not start from full-disk correlations but instead from fine surface details on an *ab initio* level, with the aim to eventually extrapolate their properties to com-

plete stellar disks. Even if most starlight originates from thermally driven granulation, the present work is necessarily incomplete as it will require future modeling of much larger structures as well (supergranulation, etc.), and also an identification of the effects of granular magnetic regions and starspots.

Fig. 7 shows correlations for jittering in radial velocity and line depth, as function of fluctuations in irradiance. These data from the ‘G2 V’ model are for four different idealized synthetic Fe I lines at $\lambda 630$ nm: weak and strong, low- and high-excitation potentials ($\chi = 1$ and 5 eV), at the two disk positions of $\mu = 1$ and 0.87, which are representative for a large fraction of the full-disk stellar flux. Each point in Fig. 7 originates from fitting the line profile averaged over the simulation area at some instance in time. The four times greater number of points for $\mu = 0.87$ reflects line profiles computed at four different azimuth angles, corresponding to observing four quadrants of the stellar disk. Similar to Fig. 6, irradiance is in units of the time-averaged disk-center continuum flux at $\lambda 630$ nm (for an example of its temporal variability, see Fig. 2 of Paper I). Because granular contrast changes with wavelength, the amplitude in irradiance must also depend on wavelength, potentially offering another diagnostic. The exact amplitude will also depends on the simulation details (e.g., the oscillation modes that are treated) and its spatial extent (see Table A.1 in Paper IV).

Obvious correlations are present: increased irradiance enhances the convective blueshift and strengthens the spectral-line absorption (presumably caused by enhanced gradients in regions of line formation). This is most pronounced for the strong line, and at stellar disk center. The values in Figs. 6-7 are from Gaussian-type functions fit to line profiles, as described above. More detailed correlation functions between fluctuating line shapes and wavelength shifts may be obtained by examining individual line profiles (Ludwig & Steffen 2008).

An estimate of the trends indicates that excursions around $\pm 100 \text{ m s}^{-1}$ correspond to about $\pm 1\%$ in irradiance. This applies to the tiny simulation patch of 5.6 Mm square (Table A.1 in Paper IV). The full solar disk is greater in effective area (recognizing the limb darkening) by a factor of $\sim 50,000$, and when we as-

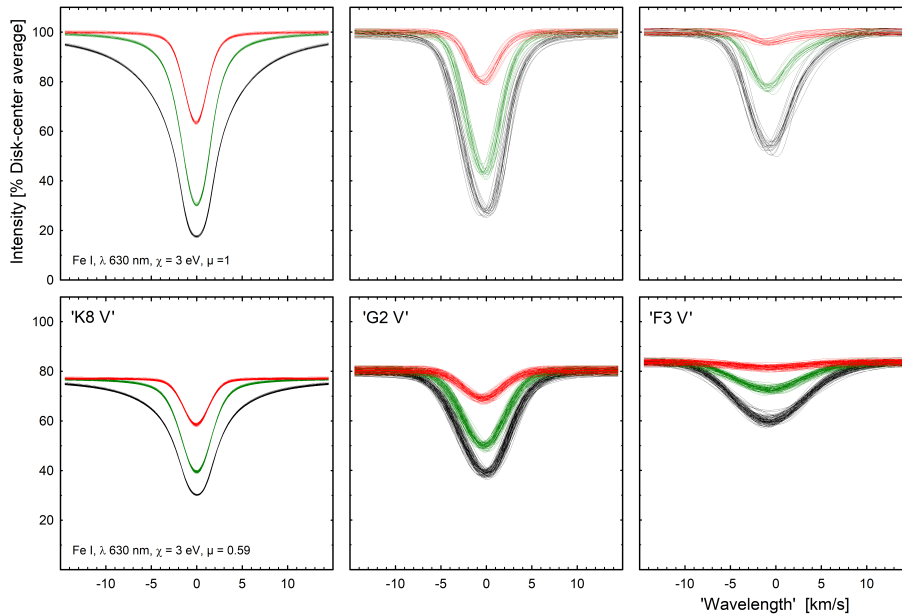


Fig. 5. Spatially averaged but temporally resolved line profiles from (left to right) the ‘K8 V’, ‘G2 V’, and ‘F3 V’ models at stellar disk center (top row) and at disk position $\mu = 0.59$ (bottom). Within each frame, spectral lines of three different strengths are shown: weak, medium and strong (red, green and black). Profiles from some 20 instances in time during the modeling sequences are plotted for an idealized Fe I line with $\chi = 3$ eV at $\lambda = 630$ nm. The number of profiles is greater for off-center data at $\mu = \cos \theta = 0.59$, which at each instance in time include profiles at four different azimuth angles (quadrants on the star). To discern the subtle variability in the ‘K8 V’ simulation, this figure should be viewed highly magnified.

sume random fluctuations and neglect center-to-limb variations, for the full disk these amplitudes would decrease by a factor $\gtrsim 200$ to about 0.5 m s^{-1} per 50 ppm in irradiance. These values are consistent with values deduced by Meunier et al. (2015) and Meunier & Lagrange (2020) for the granulation-induced signal in apparent solar full-disk radial velocity although further contributions may come from larger-scale structures such as supergranulation (Meunier & Lagrange 2019), which are not yet accessible to detailed 3D modeling. A further modeling caution is that brightness variations are also driven by p-mode oscillations which are incompletely treated in the small simulation volumes.

The most important quality is that there do exist clear correlations between fluctuations in apparent radial velocity and other parameters, which can also be precisely measured from the ground. In Fig. 7 this is shown for the line depth, normalized to the local spectral continuum. (However, absolute line depths in units of the instantaneous stellar irradiance would require measurements from space; Cegla et al. 2019.) To firmly establish the quantitative correlations, simulations over more extended areas and times are required, and also an examination of which types of spectral lines (or combinations thereof) that are most compliant. This may well differ for different stars.

From 3D simulations, not only line profiles but also broadband photometric colors can be obtained. Being less challenging than precision measurements of stellar irradiance, broad-band photometric colors can also be measured from the ground, although this requires a good understanding of atmospheric extinction. Color changes reflect stellar temperature variations and carry information analogous to flickering in brightness, supplementing line depths as another proxy for excursions in radial velocity. For CO⁵BOLD models, synthetic colors were evaluated by Bonifacio et al. (2018) and Kučinskas et al. (2018), and for the STAGGER grid by Chiavassa et al. (2018). Most probably, color indices spanning some particularly temperature-sensitive region (perhaps the G band around 415-440 nm, with its many molecular transitions) would provide the highest sensitivity.

7. Future challenges

Just as on the Sun, most of the surfaces of solar-type stars is likely covered by thermally driven patterns of granular convec-

tion, producing the spectral features discussed above and in Paper IV. However, just as on the Sun, stars also have some additional and more complex surface structures. Spatially resolved spectroscopy should be able to help distinguish the effects from at least some of these.

7.1. Stellar magnetic activity

Spectra from stellar magnetic regions are expected to display specific characteristics. On one hand, spectra retrieved from the surface regions that become temporarily hidden behind a large exoplanet during its transit will reveal the character of whatever stellar features then happened to lie behind the planet. Assuming adequate S/N can be achieved, this would enable testing the modeling and simulations of various magnetic features on different stars.

On the other hand, however, stellar activity causes challenges for the calibration of radial-velocity jittering in searches for small exoplanets. Even if satisfactory modeling of normal thermally driven granulation and fluctuations in its ensuing spectra is achieved, there remains a need to understand and segregate additional signals from time-variable magnetic activity. Adequate modeling might permit us to identify spectral signatures that are specific to different classes of magnetic features and then enable their separation. The quantitative level of the required effort strongly depends on the level of magnetic activity; for example, the Sun hosts numerous active regions during some periods but during others, it appears completely devoid of spots.

For several stars, precision photometry shows instances when the transiting planet apparently crosses some dark spot (Bruno et al. 2018; Ioannidis & Schmitt 2016a,b; Mancini et al. 2017; Močnik et al. 2017; Oshagh et al. 2013; Pont et al. 2007; Sing et al. 2011; Valio 2013), starspots can be searched for in various spectral signatures (Borra & Deschatelets 2015; Morris et al. 2020b; Reiners et al. 2013), and might perhaps be possible to glimpse with long-baseline optical interferometry (Ligi et al. 2015). Furthermore, bright flares may appear in chromospheric emission lines (Czesla et al. 2015; Klocová et al. 2017). The presence of emerging and decaying starspots complicates exoplanet discoveries (Barnes et al. 2017; Dumusque et al. 2011b; Herrero et al. 2016; Işık et al. 2018; Lagrange et al. 2010;

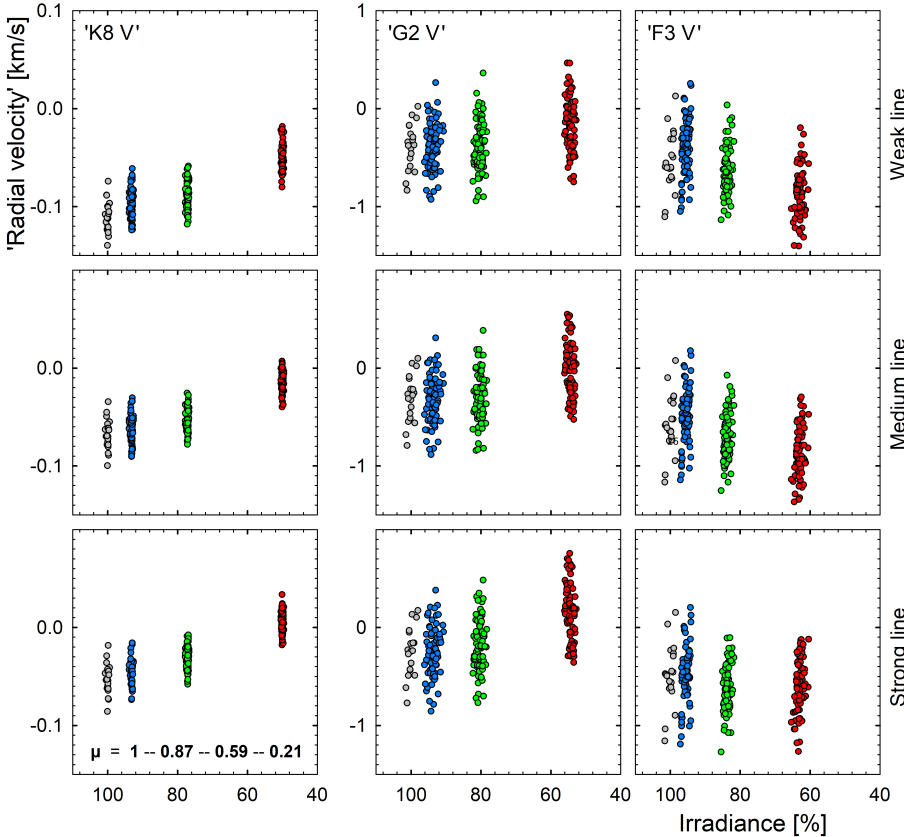


Fig. 6. Range of jittering in wavelength shift for (left to right) the ‘K8 V’, ‘G2 V’, and ‘F3 V’ models as a function of the surface irradiance at different times during each simulation. The velocity scale for the cool and quiet ‘K8 V’ model is expanded tenfold relative to the others. This plot is (from top down) for idealized weak, medium, and strong Fe I lines of $\chi = 3$ eV at $\lambda 630$ nm. The four disk positions of $\mu = 1, 0.87, 0.59$, and 0.21 are left to right inside each frame and marked in gray, blue, green and red. The number of points is four times greater for off-center positions than for $\mu = 1$ because those are sampled at four different azimuth angles. Irradiance is in units of the time-averaged disk-center continuum flux at $\lambda 630$ nm in each model.

Lanza et al. 2011; Lisogorskyi et al. 2020; Suárez Mascareño et al. 2017; Tal-Or et al. 2018), and magnetic activity cycles also add to the complications (Lovis et al. 2011). As we explained in Paper I, one of the ambitions of the current project is to recover spatially resolved spectra also of starspots and stellar magnetic regions (including Zeeman signatures in magnetically sensitive spectral lines), which requires simultaneous precision photometry to identify the exact time of starspot transit.

Here enters a certain limitation in how precisely the expected spectra can be modeled. In the cases discussed so far of thermally driven convection, the basic stellar parameters of surface gravity and effective temperature suffice to formulate a hydrodynamic problem for which ab initio simulations can be carried out. In the case of magnetically affected granulation, however, the unknown quantity of the total magnetic flux on (parts of) the stellar surface enters, which cannot be precisely measured (probably not even for the Sun). In response to transiting active regions, the Sun (seen as a star) varies in irradiance (Toriumi et al. 2020) and in apparent radial velocity (Dumusque et al. 2020). It has been suggested that the Sun is less active than other G-type stars (Reinhold et al. 2020), although other arguments exist in the literature. In any case, magnetic activity tends to decrease with age and with slower stellar rotation.

After introducing a certain magnetic flux in 3D atmospheric structures, its development can be followed into magnetic flux concentrations around intergranular lanes, the magnetic forces being balanced by gas pressure and dynamic effects. In cooler stars with higher photospheric pressures, magnetic fields can be compressed to greater flux densities than is possible on the Sun. This surface magnetohydroconvection, reproducing the appearance of distorted granulation in solar facular or plage regions, has been modeled, for example, by Beeck et al. (2015a), Khomenko et al. (2018), and Salhab et al. (2018). Spectral synthesis illustrates

how the magnetic properties are reflected in the shapes of spectral lines, depending on their magnetic sensitivity (Holzreuter & Solanki 2012, 2015). For our project, the main relevance is for spectral-line properties at various center-to-limb distances for different classes of stars (Beeck et al. 2015b).

With sufficiently strong flux concentrations, surface convection is inhibited and starspots develop, whose flux densities and other properties seem determined by basic stellar parameters. While the varying amount of magnetic flux for any one star may determine how many magnetic regions are present, it probably does not greatly affect properties of individual starspots, making them promising targets for spatially resolved spectroscopy because any single starspot should be a representative object. Quite detailed 3D magnetohydrodynamic modeling of starspot umbrae and penumbrae is becoming possible for different stellar types (Panja et al. 2020), and with spectral synthesis a logical next step, simulated data should soon become available, eventually to be compared with observed spectra of spatially resolved stellar features. For precise determinations of magnetic field strengths, pairs of spectral lines with different Zeeman sensitivities may be used (Smitha & Solanki 2017).

7.2. Future observations

Spatially resolved stellar spectroscopy requires high-fidelity spectra at high spectral resolution, with exceptionally low photometric noise, and a very stable wavelength calibration. Data like this were not commonly available in the past, but can now be obtained at a great number of spectrometers that have recently been put in operation, or are being constructed for the primary task of radial-velocity searches for exoplanets. The radial-velocity signal is obtained by cross correlating the observed cool-star spectrum with some template and the requirement for high spectral

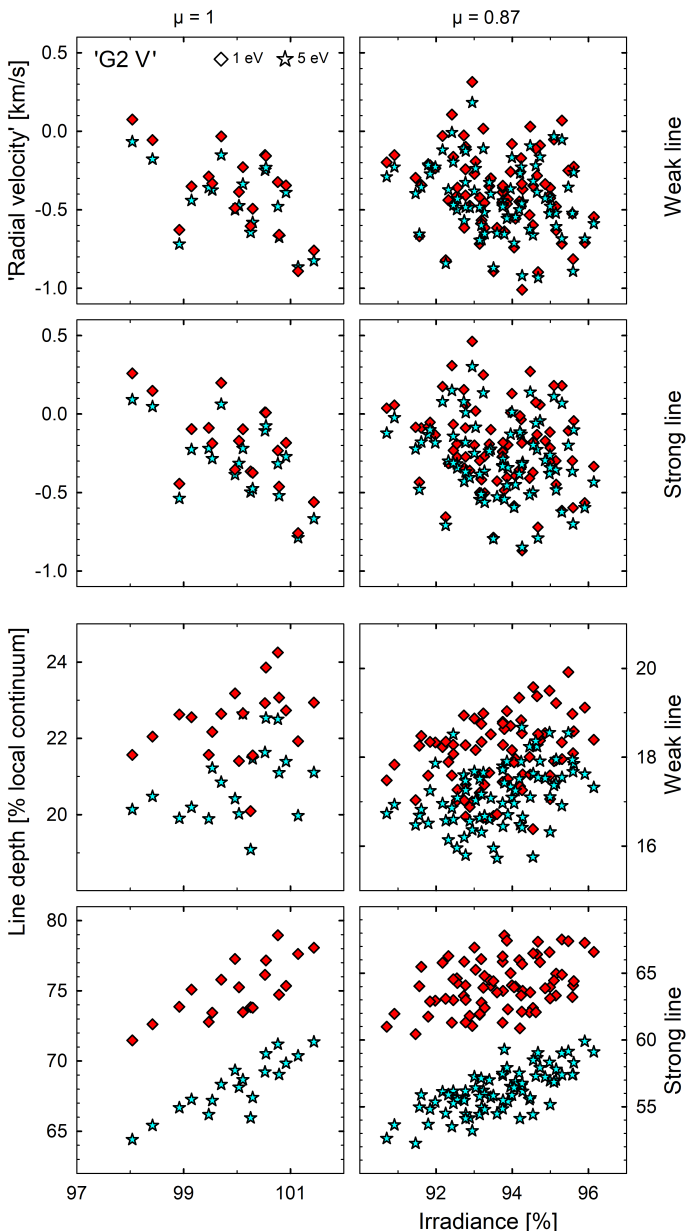


Fig. 7. Correlations between flickering in irradiance and jittering of apparent radial velocity (top) and of absorption-line depth (bottom), for differently strong lines of both low and high excitation-potentials in a solar ('G2 V') model. Measures for idealized Fe I lines at $\lambda 630$ nm are shown at stellar disk center ($\mu = 1$) and at $\mu = 0.87$; for $\chi = 1$ eV (red diamonds) and 5 eV (blue stars). The greater number of points for $\mu = 0.87$ is provided by spectra at four different azimuth angles. Irradiance is in units of the time-averaged disk-center continuum flux at $\lambda 630$ nm.

resolution follows from the need to preserve a high spectral-line contrast to produce a clear correlation signal. To reach adequate S/N, an extended spectral coverage throughout the line-rich visual range is needed, combined with a wavelength stability striving for better than 1 m s^{-1} . A few instruments operate in the near-infrared, although spectral fidelity may begin to become compromised by increased amounts of telluric absorptions. Still, the infrared may be promising for identifying signatures from stellar magnetic regions because line splitting due to the Zeeman effect increases swiftly with wavelength.

These spectra can fulfill the requirements for spatially resolved spectroscopy, as was demonstrated in Papers II and III.

Still, the spectral resolutions of almost all of these radial-velocity instruments are limited to $\sim 100,000$. As discussed above, to reveal more details of stellar photospheres, higher resolution is desirable, but there are very few suitable night-time instruments on large telescopes that also cover extended spectral ranges. Here, ESPRESSO on the ESO VLT and PEPSI on the LBT stand out, with resolutions of about 200,000 and 300,000, which will hopefully be joined by HIRES on the ESO ELT in the future (with a planned resolution of 150,000 but with details still pending).

For the illustrations in Fig. 3, the area of transiting planets was assumed as 1.5% of the stellar disk. This is the observed value for the planet transiting the G0 V star HD 209458 (Paper II), while the planet that transits the smaller K1 V star HD 189733A covers $\sim 2.5\%$ (Paper III). For smaller or larger planets, the required S/N scales inversely with planet area. Even if many spectral lines and many recordings can (and must) be averaged, perhaps from multiple transits, this stacking decreases the random noise only by the square root of the number of exposures, a slowly growing function. In practice, this limits realistic targets to host stars with transiting planets covering at least 0.5%, for instance, of their disks.

Although numerous stars are known with transiting planets of this size (Fig. 1 in Paper II), not many are also bright enough to permit truly low-noise spectra to be recorded. However, ongoing searches for bright host stars with transiting exoplanets continue to find new targets spanning rather broad temperature ranges (Bakos et al. 2020; Grieves et al. 2021; Kane et al. 2020; Lund et al. 2017; Mancini et al. 2013; Martínez et al. 2020; Pepper et al. 2013, 2020; Schrijver 2020; Wang et al. 2019, etc.). In addition to apparent stellar brightness, the suitability of a target depends on the line richness of the spectrum, and how wide a spectral range can be covered. Multiple spectral lines will have to be averaged but the extent of this averaging (as in Papers II and III) is constrained by the number and types of spectral lines that are present. Certainly, more lines than merely from Fe in the visual can be used, but if reasonably unblended lines are required from atomic species without complications of pronounced isotopic or hyperfine structure, their total number may rather be in the hundreds, not thousands. For the solar spectrum, a survey of lines from these common species (Fe I, Fe II, Ti I, Ti II, etc.) is presented in Dravins (2008). A final constraint is set by the number of detectable photons (Bouchy et al. 2001; Reiners & Zechmeister 2020), which means that these studies will greatly benefit by extremely large telescopes.

7.3. Conclusions and outlook

This survey of simulations of realistically complex spectra for stars both cooler and hotter than the Sun has identified specific 3D signatures in various categories of spectral lines that reflect the dynamic fine structure in their photospheres. This is where the spectral lines originate, whose wavelength shifts are used to infer stellar radial motion and its possible modulation by exoplanets. Current simulations treat the thermally driven surface granulation, which just as on the Sun is expected to cover most of the surface of solar-type stars and contribute the largest fraction by far of the spectral flux. The validity of these models can be tested with spatially resolved stellar spectroscopy, where stellar line profiles are retrieved from behind transiting exoplanets. While ordinary granulation produces the main patterns of convective wavelength shifts, additional contributions are expected from large-scale structures such as supergranulation or meridional flows, and from regions of magnetically affected granulation as well as starspots. Although large-volume stellar simula-

tions are challenging, they are expected eventually to be able to model supergranulation as well, while spatially resolved spectroscopy of starspots will be enabled when some exoplanet happens to transit them.

One conclusion is that when the spectral resolution $\lambda/\Delta\lambda$ reaches $\sim 100,000$, the instrumental degradation of the overall line parameters of width, depth and wavelength position is substantially smaller than the expected physical changes across stellar disks (Fig. 2). This enables the testing of atmospheric 3D models by spatially resolved spectroscopy already from the fitting of somewhat noisy data, as also demonstrated in Papers II and III. However, distinguishing the altering bisector shapes between different classes of spectral lines in any one star appears to require extremely high S/Ns (Fig. 3), likely requiring data from future extremely large telescopes.

The temporal variability of spectral line parameters can be predicted from such ab initio simulations. Because different parameters vary together, proxies can be identified for the jittering of apparent radial velocity. When these quantities can be practically measured from the ground, they should provide a means to adjust measured velocities to true stellar radial motion. In particular, the jittering in apparent radial velocity correlates with fluctuations in line depth and of photometric color (Figs. 6-7). With a sufficient physical understanding of the detailed line formation processes in stellar photospheres, it should eventually become possible to also identify truly Earth-like planets.

Acknowledgements. The work by DD is supported by grants from The Royal Physiographic Society of Lund. HGL gratefully acknowledges financial support by the Deutsche Forschungsgemeinschaft (DFG, German Research Foundation) – Project ID 138713538–SFB 881 (‘The Milky Way System’, subproject A04). Use was made of NASA’s ADS Bibliographic Services and the arXiv® distribution service. We thank the referee, Andrea Chiavassa, for his detailed and insightful comments.

References

Adibekyan, V., Sousa, S. G., Santos, N. C., et al. 2020, *A&A*, 642, A182.

Albrecht, S. 2012, *IAU Symp.*, 282, 379

Allende Prieto, C., Asplund, M., García López, R. J., & Lambert, D. L. 2002, *ApJ*, 567, 544

Apai, D., Rackham, B. V., Giampapa, M. S., et al. 2018, arXiv:1803.08708

Asplund, M. 2005, *ARA&A*, 43, 481

Asplund, M., Nordlund, Å., Trampedach, R., Allende Prieto, C., & Stein, R. F. 2000, *A&A*, 359, 729

Bakos, G. A., Hartman, J. D., Bhatti, W., et al. 2020, arXiv:2007.05528

Barnes, J. R., Jeffers, S. V., Anglada-Escudé, G., et al. 2017, *MNRAS*, 466, 1733

Bastien, F. A., Stassun, K. G., Basri, G., et al. 2016, *ApJ*, 818, 43

Bechter, A. J., Bechter, E. B., Crepp, J. R., et al. 2018, *Proc. SPIE*, 10702, 107026T

Beckers, J. M., Andersen, T. E., & Owner-Petersen, M. 2007, *Optics Express*, 15, 1983

Beeck, B., Schüssler, M., Cameron, R. H., et al. 2015a, *A&A*, 581, A42

Beeck, B., Schüssler, M., Cameron, R. H., et al. 2015b, *A&A*, 581, A43

Benatti, S. 2018, *Geosciences*, 8, 289

Bergemann, M., Gallagher, A. J., Eitner, P., et al. 2019, *A&A*, 631, A80

Blackman, R. T., Fischer, D. A., Jurgenson, C. A., et al. 2020, *AJ*, 159, 238

Bonifacio, P., Caffau, E., Ludwig, H.-G., et al. 2018, *A&A*, 611, A68

Borra, E. F. & Deschatelets, D. 2015, *AJ*, 150, 146

Bouchy, F., Pepe, F., & Queloz, D. 2001, *A&A*, 374, 733

Brewer, J. M., Fischer, D. A., Blackman, R. T., et al. 2020, *AJ*, 160, 67

Bruno, G., Lewis, N. K., Stevenson, K. B., et al. 2018, *AJ*, 156, 124

Cale, B., Plavchan, P., LeBrun, D., et al. 2019, *AJ*, 158, 170

Cegla, H. 2019, *Geosciences*, 9, 114

Cegla, H. M., Stassun, K. G., Watson, C. A., et al. 2014, *ApJ*, 780, 104

Cegla, H. M., Oshagh, M., Watson, C. A., et al. 2016, *ApJ*, 819, 67

Cegla, H. M., Watson, C. A., Shelyag, S., et al. 2019, *ApJ*, 879, 55

Chiavassa, A. & Brogi, M. 2019, *A&A*, 631, A100

Chiavassa, A., Casagrande, L., Collet, R., et al. 2018, *A&A*, 611, A11

Collier Cameron, A., Mortier, A., Phillips, D., et al. 2019, *MNRAS*, 487, 1082

Collier Cameron, A., Ford, E. B., Shahaf, S., et al. 2020, arXiv:2011.00018

Cranmer, S. R., Bastien, F. A., Stassun, K. G., et al. 2014, *ApJ*, 781, 124

Crass, J., Bechter, A., Bechter, E., et al. 2019, *BAAS*, 51, 122

Cretignier, M., Dumusque, X., Allart, R., et al. 2020, *A&A*, 633, A76

Crossfield, I. J. M. 2014, *A&A*, 566, A130

Czesla, S., Klocová, T., Khalafinejad, S., Wolter, U., & Schmitt, J. H. M. M. 2015, *A&A*, 582, A51

de Beurs, Z. L., Vanderburg, A., Shallue, C. J., et al. 2020, arXiv:2011.00003

de Laeter, J. R., Böhle, J. K., de Bièvre, P., et al. 2003, *Pure. Appl. Chem.* 75, 683

Dravins, D. 2008, *A&A*, 492, 199

Dravins, D., & Nordlund, Å. 1990, *A&A*, 228, 184

Dravins, D., Ludwig, H.-G., Dahlén, E., & Pazira, H. 2017a, *A&A*, 605, A90 (Paper I)

Dravins, D., Ludwig, H.-G., Dahlén, E., & Pazira, H. 2017b, *A&A*, 605, A91 (Paper II)

Dravins, D., Gustavsson, M., Ludwig, H.-G. 2018, *A&A*, 616, A144 (Paper III)

Dravins, D., Ludwig, H.-G. & Freytag, B. 2021, *A&A*, accepted (Paper IV)

Dumusque, X. 2016, *A&A*, 593, A5

Dumusque, X. 2018, *A&A*, 620, A47

Dumusque, X., Udry, S., Lovis, C., et al. 2011a, *A&A*, 525, A140

Dumusque, X., Santos, N. C., Udry, S., et al. 2011b, *A&A*, 527, A82

Dumusque, X., Glenday, A., Phillips, D. F., et al. 2015, *ApJ*, 814, L21

Dumusque, X., Cretignier, M., Sosnowska, D., et al. 2020, arXiv:2009.01945

Feng, F., Tuomi, M., Jones, H. R. A., et al. 2016, *MNRAS*, 461, 2440

Fischer, D. A., Anglada-Escudé, G., Arriagada, P., et al. 2016, *PASP*, 128, 066001

Freytag, B., Steffen, M., Ludwig, H.-G., et al. 2012, *J. Comp. Phys.*, 231, 919

Gilbert, J., Bergmann, C., Bloxham, G., et al. 2018, *Proc. SPIE*, 10702, 107020Y

González Hernández, J. I., Pepe, F., Molaro, P., et al. 2018, *Handbook of Exoplanets*, 157

Grieves, N., Nielsen, L. D., Vines, J. I., et al. 2021, arXiv:2101.04245

Hall, R. D., Thompson, S. J., Handley, W., et al. 2018, *MNRAS*, 479, 2968

Halverson, S., Terrien, R., Mahadevan, S., et al. 2016, *Proc. SPIE*, 9908, 99086P

Haywood, R. D., Collier Cameron, A., Unruh, Y. C., et al. 2016, *MNRAS*, 457, 3637

Herrero, E., Ribas, I., Jordi, C., et al. 2016, *A&A*, 586, A131

Hojjatpanah, S., Oshagh, M., Figueira, P., et al. 2020, *A&A*, 639, A35

Holzreuter, R. & Solanki, S. K. 2012, *A&A*, 547, A4

Holzreuter, R. & Solanki, S. K. 2015, *A&A*, 582, A101

Ioannidis, P. & Schmitt, J. H. M. M. 2016a, *A&A*, 594, A41

Ioannidis, P. & Schmitt, J. H. M. M. 2016b, *A&A*, 594, A42

İşik, E., Solanki, S. K., Krivova, N. A., et al. 2018, *A&A*, 620, A177

İşik, E., Shapiro, A. I., Solanki, S. K., et al. 2020, *ApJ*, 901, L12

Jovanovic, N., Beichman, C., Blake, C., et al. 2019, *BAAS*, 51, 270

Kallinger, T., De Ridder, J., Hekker, S., et al. 2014, *A&A*, 570, A41

Kane, S. R., Yalçınkaya, S., Osborn, H. P., et al. 2020, *AJ*, 160, 129

Khomenko, E., Vitas, N., Collados, M., et al. 2018, *A&A*, 618, A87

Klocová, T., Czesla, S., Khalafinejad, S., Wolter, U., & Schmitt, J. H. M. M. 2017, *A&A*, 607, A66

Korhonen, H., Andersen, J. M., Piskunov, N., et al. 2015, *MNRAS*, 448, 3038

Kosiarek, M. R. & Crossfield, I. J. M. 2020, *AJ*, 159, 271

Kučinskas, A., Klevas, J., Ludwig, H.-G., et al. 2018, *A&A*, 613, A24

Lagrange, A.-M., Desort, M., & Meunier, N. 2010, *A&A*, 512, A38

Langellier, N., Milbourne, T. W., Phillips, D. F., et al. 2020, arXiv:2008.05970

Lanza, A. F., Boisse, I., Bouchy, F., et al. 2011, *A&A*, 533, A44

Lanza, A. F., Molaro, P., Monaco, L., et al. 2016, *A&A*, 587, A103

Lanza, A. F., Collier Cameron, A., & Haywood, R. D. 2019, *MNRAS*, 486, 3459

Ligi, R., Mourard, D., Lagrange, A.-M., et al. 2015, *A&A*, 574, A69

Lisogorskyi, M., Saikia, S. B., Jeffers, S. V., et al. 2020, *MNRAS*, 497, 4009

Lo Curto, G., Manescu, A., Avila, G., et al. 2012, *Proc. SPIE*, 8446, 84461W

Löhner-Böttcher, J., Schmidt, W., Stief, F., et al. 2018, *A&A*, 611, A4

Löhner-Böttcher, J., Schmidt, W., Schlichenmaier, R., et al. 2019, *A&A*, 624, A57

Lovis, C., Dumusque, X., Santos, N. C., et al. 2011, arXiv:1107.5325

Ludwig, H.-G. & Steffen, M. 2008, *Precision Spectroscopy in Astrophysics*, 133. doi:10.1007/978-3-540-75485-5_29

Ludwig, H.-G., Koesterke, L., Allende Prieto, C., et al. 2021, *A&A*, to be submitted

Luhm, J. K., Wright, J. T., Howard, A. W., et al. 2020a, *AJ*, 159, 235

Luhm, J. K., Wright, J. T., & Isaacson, H. 2020b, *AJ*, 159, 236

Lund, M. B., Rodriguez, J. E., Zhou, G., et al. 2017, *AJ*, 154, 194

Lundkvist, M. S., Ludwig, H.-G., Collet, R., et al. 2021, *MNRAS*, 501, 2512

Maldonado, J., Phillips, D. F., Dumusque, X., et al. 2019, *A&A*, 627, A118

Mancini, L., Southworth, J., Ciceri, S., et al. 2013, *A&A*, 551, A11

Mancini, L., Southworth, J., Raia, G., et al. 2017, *MNRAS*, 465, 843

Marchwinski, R. C., Mahadevan, S., Robertson, P., et al. 2015, *ApJ*, 798, 63

Marconi, A., Di Marcantonio, P., D’Odorico, V., et al. 2016, *Proc. SPIE*, 9908, 990823

Marconi, A., Abreu, M., Adibekyan, V., et al. 2021, *The Messenger*, 182, 27

Martínez, R. R., Gaudi, B. S., Rodriguez, J. E., et al. 2020, *AJ*, 160, 111

Metcalf, A. J., Anderson, T., Bender, C. F., et al. 2019, *Optica*, 6, 233

Meunier, N. & Lagrange, A.-M. 2019, *A&A*, 625, L6

Meunier, N. & Lagrange, A. M. 2020, *A&A*, 642, A157

Meunier, N., Desort, M., & Lagrange, A.-M. 2010, *A&A*, 512, A39

Meunier, N., Lagrange, A.-M., Borgniet, S., et al. 2015, *A&A*, 583, A118

Meunier, N., Lagrange, A.-M., Mbemba Kabuiku, L., et al. 2017a, *A&A*, 597, A52

Meunier, N., Lagrange, A.-M., & Borgniet, S. 2017b, *A&A*, 607, A6

Miklos, M., Milbourne, T. W., Haywood, R. D., et al. 2020, *ApJ*, 888, 117

Milbourne, T. W., Haywood, R. D., Phillips, D. F., et al. 2019, *ApJ*, 874, 107

Močnik, T., Hellier, C., Anderson, D. R., et al. 2017, *MNRAS*, 469, 1622

Morris, B. M., Bobra, M. G., Agol, E., et al. 2020, *MNRAS*, 493, 5489

Morris, B. M., Hoeijmakers, H. J., Kitzmann, D., et al. 2020b, *AJ*, 160, 5

Némec, N.-E., İşık, E., Shapiro, A. I., et al. 2020, *A&A*, 638, A56

Nordlund, Å., Stein, R. F., & Asplund, M. 2009, *Living Rev. Solar Phys.*, 6, 2

Norris, C. M., Beeck, B., Unruh, Y. C., et al. 2017, *A&A*, 605, A45

Oshagh, M., Santos, N. C., Boisse, I., et al. 2013, *A&A*, 556, A19

Oshagh, M., Santos, N. C., Figueira, P., et al. 2017, *A&A*, 606, A107

Pande, D., Bedding, T. R., Huber, D., et al. 2018, *MNRAS*, 480, 467

Panja, M., Cameron, R., & Solanki, S. K. 2020, *ApJ*, 893, 113

Pasquini, L., Cristiani, S., García López, R., et al. 2010, *Proc. SPIE*, 7735, 77352F

Pepe, F., Molaro, P., Cristiani, S., et al. 2014, *Astron. Nachr.*, 335, 8

Pepe, F., Cristiani, S., Rebolo, R., et al. 2021, *A&A*, 645, A96

Pepper, J., Siverd, R. J., Beatty, T. G., et al. 2013, *ApJ*, 773, 64

Pepper, J., Kane, S. R., Rodriguez, J. E., et al. 2020, *AJ*, 159, 243

Perryman, M. 2018, *The Exoplanet Handbook*, Cambridge Univ. Press; 2nd ed., ISBN: 9781108419772

Petersburg, R. R., Ong, J. M. J., Zhao, L. L., et al. 2020, *AJ*, 159, 187

Plavchan, P., Vasishth, G., Beichman, C., et al. *EarthFinder Probe Mission Concept Study*, NASA-JPL-George Mason University-Caltech, 66 pp. 2019, arXiv:2006.13428

Pont, F., Gilliland, R. L., Moutou, C., et al. 2007, *A&A*, 476, 1347

Probst, R. A., Milaković, D., Toledo-Padrón, B., et al. 2020, *Nature Astronomy*, 4, 603

Rackham, B. V., Apai, D., & Giampapa, M. S. 2018, *ApJ*, 853, 122

Rackham, B. V., Apai, D., & Giampapa, M. S. 2019, *AJ*, 157, 96

Reiners, A. & Zechmeister, M. 2020, *ApJS*, 247, 11

Reiners, A., Shulyak, D., Anglada-Escudé, G., et al. 2013, *A&A*, 552, A103

Reiners, A., Lemke, U., Bauer, F., Beeck, B., & Huke, P. 2016, *A&A*, 595, A26

Reinhold, T., Shapiro, A. I., Solanki, S. K., et al. 2020, *Science*, 368, 518

Robertson, J. G. 2013, *PASA*, 30, e048

Robertson, P., Anderson, T., Stefansson, G., et al. 2019, *Journal of Astronomical Telescopes, Instruments, and Systems*, 5, 015003

Roy, A., Chakraborty, A., Mahadevan, S., et al. 2016, *Proc. SPIE*, 9908, 99086R

Salhab, R. G., Steiner, O., Berdyugina, S. V., et al. 2018, *A&A*, 614, A78

Samadi, R., Belkacem, K., & Ludwig, H.-G. 2013a, *A&A*, 559, A39

Samadi, R., Belkacem, K., Ludwig, H.-G., et al. 2013b, *A&A*, 559, A40

Sarkar, S., Argyriou, I., Vandenbussche, B., et al. 2018, *MNRAS*, 481, 2871

Schrijver, C. J. 2020, *ApJ*, 890, 121

Shporer, A., & Brown, T. 2011, *ApJ*, 733, 30

Sing, D. K., Pont, F., Aigrain, S., et al. 2011, *MNRAS*, 416, 1443

Smitha, H. N. & Solanki, S. K. 2017, *A&A*, 608, A111

Strassmeier, K. G., Ilyin, I., Järvinen, A., et al. 2015, *Astron. Nachr.*, 336, 324

Strassmeier, K. G., Ilyin, I., & Steffen, M. 2018a, *A&A*, 612, A44

Strassmeier, K. G., Ilyin, I., & Weber, M. 2018b, *A&A*, 612, A45

Suárez Mascareño, A., Rebolo, R., González Hernández, J. I., et al. 2017, *MNRAS*, 468, 4772

Suárez Mascareño, A., Faria, J. P., Figueira, P., et al. 2020, *A&A*, 639, A77

Sulis, S., Mary, D., & Bigot, L. 2020a, *A&A*, 635, A146

Sulis, S., Lendl, M., Hofmeister, S., et al. 2020b, *A&A*, 636, A70

Tal-Or, L., Zechmeister, M., Reiners, A., et al. 2018, *A&A*, 614, A122

Tayar, J., Stassun, K. G., & Corsaro, E. 2019, *ApJ*, 883, 195

Thompson, A. P. G., Watson, C. A., Haywood, R. D., et al. 2020, *MNRAS*, 494, 4279

Toriumi, S., Airapetian, V. S., Hudson, H. S., et al. 2020, *ApJ*, 902, 36

Trampedach, R., Asplund, M., Collet, R., et al. 2013, *ApJ*, 769, 18

Valio, A. 2013, *New Quests in Stellar Astrophysics III: A Panchromatic View of Solar-Like Stars, With and Without Planets*, ASPC 472, 239

Wang, S., Jones, M., Shporer, A., et al. 2019, *AJ*, 157, 51

Wilken, T., Curto, G. L., Probst, R. A., et al. 2012, *Nature*, 485, 611

Winn, J. N. 2011, *IAU Symp. 276, The Astrophysics of Planetary Systems: Formation, Structure, and Dynamical Evolution*, 230

Yan, F., Fosbury, R. A. E., Petr-Gotzens, M. G., Pallé, E., & Zhao, G. 2015a, *ApJ*, 806, L23

Yan, F., Fosbury, R. A. E., Petr-Gotzens, M. G., Zhao, G., & Pallé, E. 2015b, *A&A*, 574, A94

Yan, F., Pallé, E., Fosbury, R. A. E., Petr-Gotzens, M. G., & Henning, T. 2017, *A&A*, 603, A73

Zerbi, F. M., Bouchy, F., Fynbo, J., et al. 2014, *Proc. SPIE*, 9147, 914723

Zhao, F., Lo Curto, G., Pasquini, L., et al. 2021, *A&A*, 645, A23